

www.acsnano.org

# Binding of Benzo[a]pyrene Alters the Bioreactivity of Fine Biochar Particles toward Macrophages Leading to Deregulated Macrophagic Defense and Autophagy

Juan Ma,<sup>#</sup> Xinlei Liu,<sup>#</sup> Yi Yang, Jiahuang Qiu, Zheng Dong, Quanzhong Ren, Yi Y. Zuo, Tian Xia, Wei Chen,\* and Sijin Liu\*



Cite This: ACS Nano 2021, 15, 9717-9731



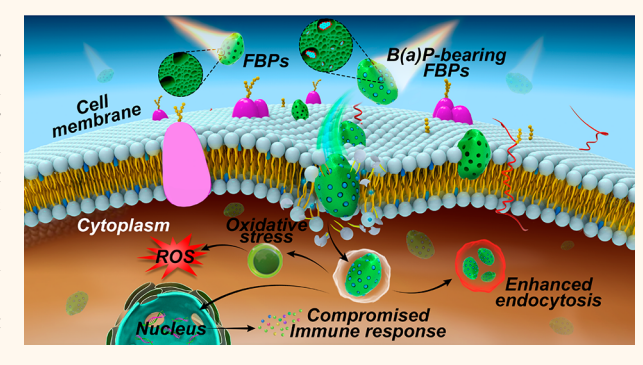
**ACCESS** 

III Metrics & More

Article Recommendations

s Supporting Information

ABSTRACT: Contaminant-bearing fine biochar particles (FBPs) may exert significantly different toxicity profiles from their contaminant-free counterparts. While the role of FBPs in promoting contaminant uptake has been recognized, it is unclear whether the binding of contaminants can modify the biochemical reactivity and toxicological profiles of FBPs. Here, we show that binding of benzo[a]pyrene (B(a)P, a model polycyclic aromatic hydrocarbon) at environmentally relevant exposure concentrations markedly alters the cytotoxicity of FBPs to macrophages, an important line of innate immune defense against airborne particulate matters (PMs). Specifically, B(a)P-bearing FBPs elicit more severe disruption of the phospholipid membrane, endocy-



tosis, oxidative stress, autophagy, and compromised innate immune defense, as evidenced by blunted proinflammatory effects, compared with B(a)P-free FBPs. Notably, the altered cytotoxicity cannot be attributed to the dissolution of B(a)P from the B(a)P-bearing FBPs, but appears to be related to B(a)P adsorption-induced changes of FBPs bioreactivity toward macrophages. Our findings highlight the significance of environmental chemical transformation in altering the bioreactivity and toxicity of PMs and call for further studies on other types of carbonaceous nanoparticles and additional exposure scenarios.

**KEYWORDS:** natural nanoparticles, fine biochar particles, benzo[a]pyrene adsorption, bioreactivity, macrophages

ine biochar particles (FBPs) are a major source of carbonaceous airborne particulate matters (PMs) mainly originated from the pyrolysis of agricultural biomass under oxygen-limited conditions. Additionally, application of biochar materials in farmlands or contaminated sites releases large quantities of micro- and nanosized biochar particles, 1-3 a significant portion of which may enter the atmospheric environment as dusts. 4,5 Accordingly, the abundance of FBPs in the environment is much higher than that of engineered nanoparticles.<sup>5</sup> FBPs can actively participate in atmospheric photochemical reactions, resulting in the formation of atmospheric aerosols, and can pose ecotoxicological<sup>6-8</sup> and human respiratory risks.<sup>5,9</sup> Owing to their large surface area, porous structures, aromaticity, and surface oxygen-functionality, FBPs can accumulate various organic contaminants (e.g., polycyclic aromatic hydrocarbons (PAHs) and heavy metals), either during pyrolysis or in the

environment (e.g., through adsorption of contaminants from the aqueous solutions). Accordingly, the toxicological effects of contaminant-bearing FBPs should be attributed to the combined effects of both FBPs and the contaminants associated with these particles.

Although a number of studies have been conducted to understand the joint toxicities of FBPs and organic contaminants (in particular, PAHs), 9,15-17 most focused on how FBPs may affect the bioaccessibility of the contaminants being carried. The most accepted mechanism is the "Trojan-

Received: January 12, 2021 Accepted: June 7, 2021 Published: June 14, 2021





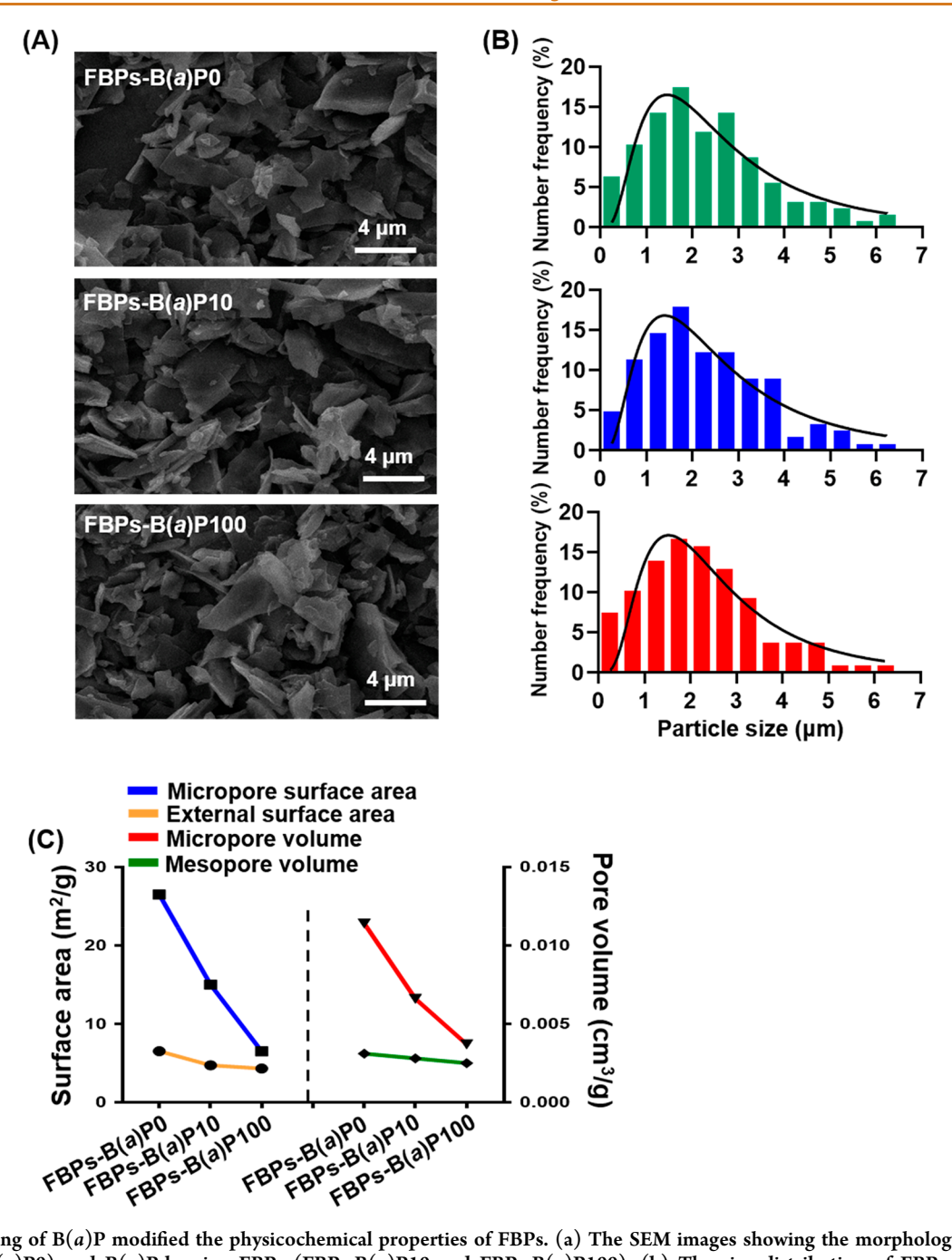


Figure 1. Loading of B(a)P modified the physicochemical properties of FBPs. (a) The SEM images showing the morphology of B(a)P-free FBPs (FBPs-B(a)P0) and B(a)P-bearing FBPs (FBPs-B(a)P10) and FBPs-B(a)P100). (b) The size distribution of FBPs determined by measuring more than 200 particles in the SEM images. (c) Quantification of surface area and micropore/mesopore volume of FBPs.

horse" effect, that is, FBPs carry and deliver PAHs to promote the cellular uptake of these contaminant compounds, thus increasing the intracellular bioaccessibility of PAHs. In comparison, little is known about how the binding of contaminants might alter the toxicity profiles of the particles. Here, we speculate that adsorption of contaminants can modify the bioreactivity of FBPs and, consequently, may alter the toxicological profiles of FBPs. To test this hypothesis, we examined the effects of PAH adsorption on the cytotoxicity of FBPs to J774.A1 macrophages, including disruption of phospholipid membranes, endocytosis, oxidative stress response, autophagy, and proinflammatory effects. The findings unravel a previously unrecognized toxicity mechanism of contaminant-bearing PMs, that is, the binding of contaminants

to PMs affects their interaction with the target cells. This work has important implications for the risk assessment of both naturally occurring nanoparticles and engineered nanomaterials.

## **RESULTS AND DISCUSSION**

Binding of PAHs Modified the Physicochemical Properties of FBPs. FBPs were obtained by combusting corn straw and wheat stalk (Wh) at 500  $^{\circ}$ C under oxygen-limited conditions. The FBPs derived from corn straw were used as the primary material and were referred to as FBPs hereafter. The FBPs from wheat stalk were used as the supporting materials and were noted as FBPs-Wh. Benzo[a]-pyrene (B(a)P), phenanthrene (Phe), and pyrene (Pyr), three

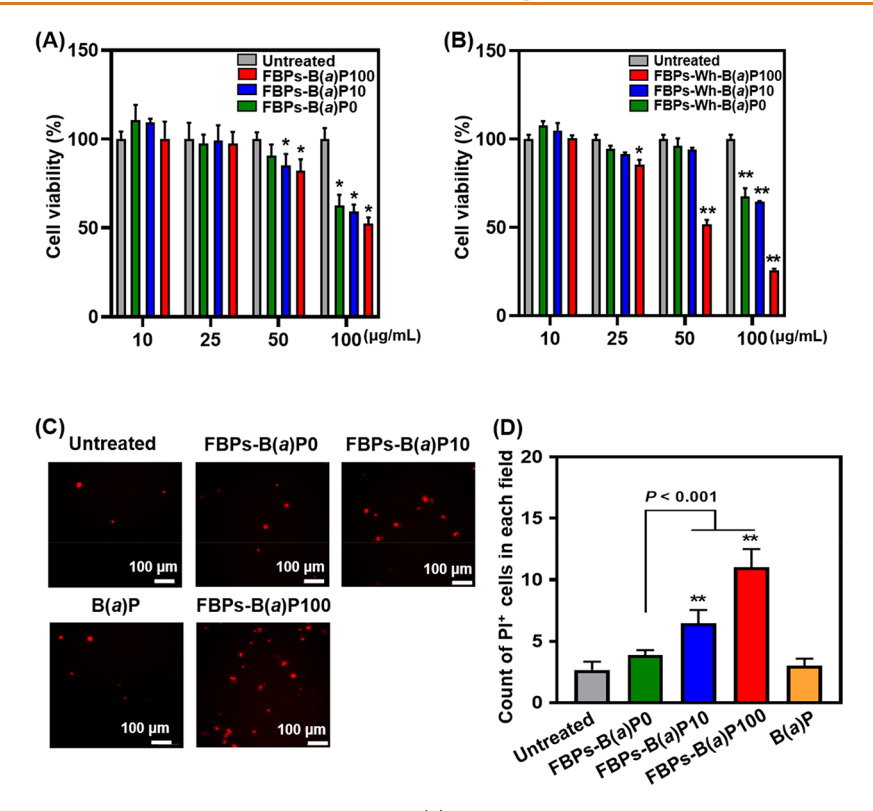


Figure 2. B(a)P-bearing FBPs caused more significant cell death. (a) Cell viability of J774.A1 cells upon exposure to pristine FBPs and B(a)P-bearing FBPs at 10, 25, 50, and 100  $\mu$ g/mL (determined by the mass concentration of FBPs) for 24 h (n = 6). (b) Cell viability of J774.A1 cells after treatment with pristine FBPs-Wh and B(a)P-bearing FBPs-Wh at 10, 25, 50, and 100  $\mu$ g/mL for 24 h (n = 6). The exposure concentration of each particle was determined by the mass concentration of FBPs-Wh. (c) The PI staining of J774.A1 cells upon pristine FBPs and B(a)P-bearing FBP treatment at 50  $\mu$ g/mL (determined by the mass concentration of FBPs) for 24 h (n = 4). Based on the maximum dissolution efficacy of B(a)P from B(a)P-bearing FBPs in culture medium, namely <10%, as described in Supplementary Figure 3B, the concentration of dissolved B(a)P from B(a)P-bearing FBPs was only 0.5  $\mu$ g/L. To this end, a maximum value, 5  $\mu$ g/L, was used as the control of potential freed B(a)P. (d) Quantitative analysis of cell death based on PI staining. The number of PI<sup>+</sup> cells in six randomly selected fields in each image was calculated. P < 0.05 (\*) relative to the untreated control. P < 0.001 (\*\*) relative to the untreated control.

of the most abundant PAHs on FBPs, 18 were loaded to FBPs, using a volatile organic solvent drying method to mimic the accumulation of PAHs during combustion 19-21 (this method was used in previous studies for the loading of PAHs onto carbonaceous particles such as carbon black particles).21-24 The PAH-bearing FBPs contained 10 or 100  $\mu$ g/g PAH, respectively, to represent the commonly observed PAH loadings in environmental samples. 18,25 A numerical number 10 or 100 was added to the acronym of a sample to indicate the concentration of PAH (for example, the wheat-derived FBP sample containing 10  $\mu$ g/g B(a)P was referred to as FBPs-Wh-B(a)P10, and the corn-derived FBP sample containing 100  $\mu$ g/g pyrene was named FBPs-Pyr100). The PAH-free FBPs, used as the control samples, were obtained by going through the same PAH-loading procedures but without adding any PAH. These samples were identified with a numerical number 0 (e.g., FBPs-B(a)P0 and FBPs-Wh-

The scanning electron microscopy (SEM) images showed that the B(a)P-bearing FBPs manifested the similar thin-sheet-like morphology to that of FBPs-B(a)P0 and B(a)P-free FBPs (Figure 1A). A similar size distribution profile was observed for FBPs-B(a)0, FBPs-B(a)P10, and FBPs-B(a)P100, with an average lateral size of around 2.2  $\mu$ m (Figure 1B); the size distribution profiles of FBPs-Wh-B(a)P100, FBPs-Phe100 and FBPs-Pyr100 were also comparable (Supplementary Figure 1).

As demonstrated previously, 26-29 FBPs have large surface areas and contain pores of various sizes. Thus, FBPs exhibit a high adsorption affinity and capacity for organic pollutants (e.g., PAHs), by allowing not only surface adsorption but also micropore filling. Strikingly, the micropore surface areas of FBPs-B(a)P10 and FBPs-B(a)P100 (15 and 6.5  $m^2/g$ ) were 43% and 75% smaller than that of FBPs-B(a)P0 (26.5  $m^2/g$ ) (Figure 1C, P < 0.001) and consistent with the smaller micropore/mesopore volumes of FBPs-B(a)P10 and FBPs-B(a)P100 (Figure 1C, P < 0.001). The external surface areas of the FBPs-B(a)P10 and FBPs-B(a)P100 were also smaller than FBPs-B(a)P0, even though to a lesser degree (Figure 1C). The smaller micropore volumes and surface areas of the FBPs-B(a)P10 and FBPs-B(a)P100 were in line with the micropore-filling mechanism, 30-32 in that micropore regions are the preferable adsorption sites for PAHs.<sup>31</sup> The molecular dimension of B(a)P (Supplementary Figure 2) (1.3740 nm  $\times$  0.9197 nm  $\times$  0.3886 nm) allowed B(a)P molecules to enter the micropores, wherein the molecules can interact with multiple pore walls, resulting in enhanced adsorption, and thus, adsorption of B(a)P in the micropores of FBPs is thermodynamically more stable. The adsorption of B(a)Pmolecules in the micropores likely hindered the entrance of N<sub>2</sub> to the pores during the  $N_2$  adsorption process, as supported by the high loading efficacy (essentially 100%) of B(a)P onto FBPs-B(a)P10 and FBPs-B(a)P100 (Supplementary Figure

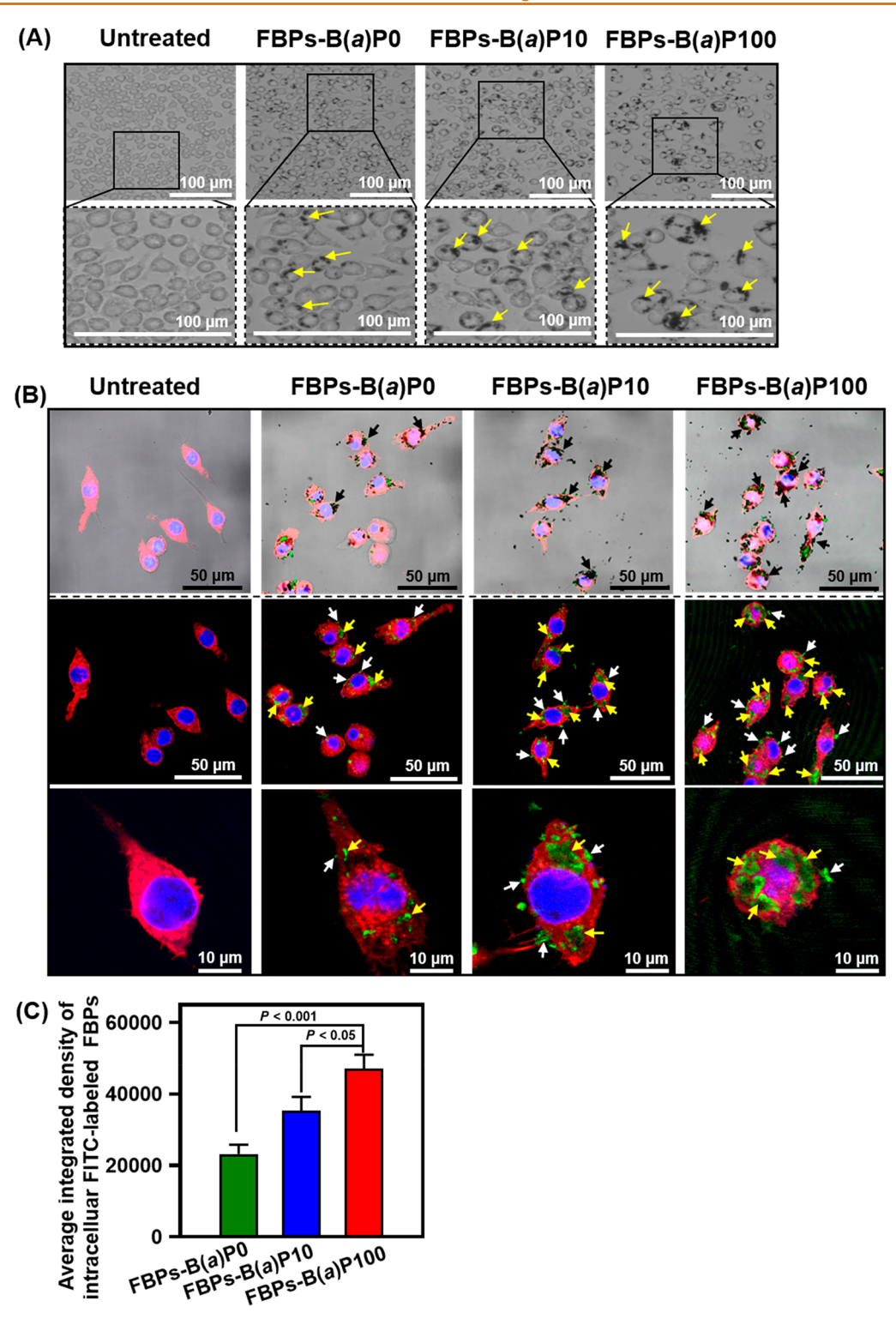


Figure 3. B(a)P-bearing FBPs incurred greater association with the plasma membrane and cellular internalization. (a) Determination of cellular morphology and particle—bio interactions. Phase-contrast images show the morphological alterations of J774.A1 cells treated with  $10 \,\mu \text{g/mL}$  (determined by the mass concentration of FBPs) pristine FBPs and B(a)P-bearing FBPs for 48 h. The enlarged views of the cells are shown in the lower panel (scale bar:  $100 \,\mu \text{m}$ ). The ingested FBPs inside the cells are indicated by yellow arrows. (b) Visualization of FBP localization. FITC-BSA-labeled FBP (in green) after treatment for 6 h was visualized through confocal laser scanning microscopy. The cell membrane was stained with rhodamine-phalloidin in red, and cell nuclei were counter-stained with DAPI in blue. The upper panel represents the merged images based on the bright field and fluorescence field. Fluorescent images are presented in the middle panel, and enlarged images are shown in the bottom panel (scale bar:  $10 \,\mu \text{m}$ ). Black arrows point at the FBPs. Yellow arrows indicate FBPs within the cytoplasm. White arrows denote FBPs in association with the surface of the plasma membrane. (c) Quantitative data of the intracellular FITC-labeled FBPs. The immunofluorescent intensity was quantified using the ImageJ software by randomly selecting 30 fields in each image.

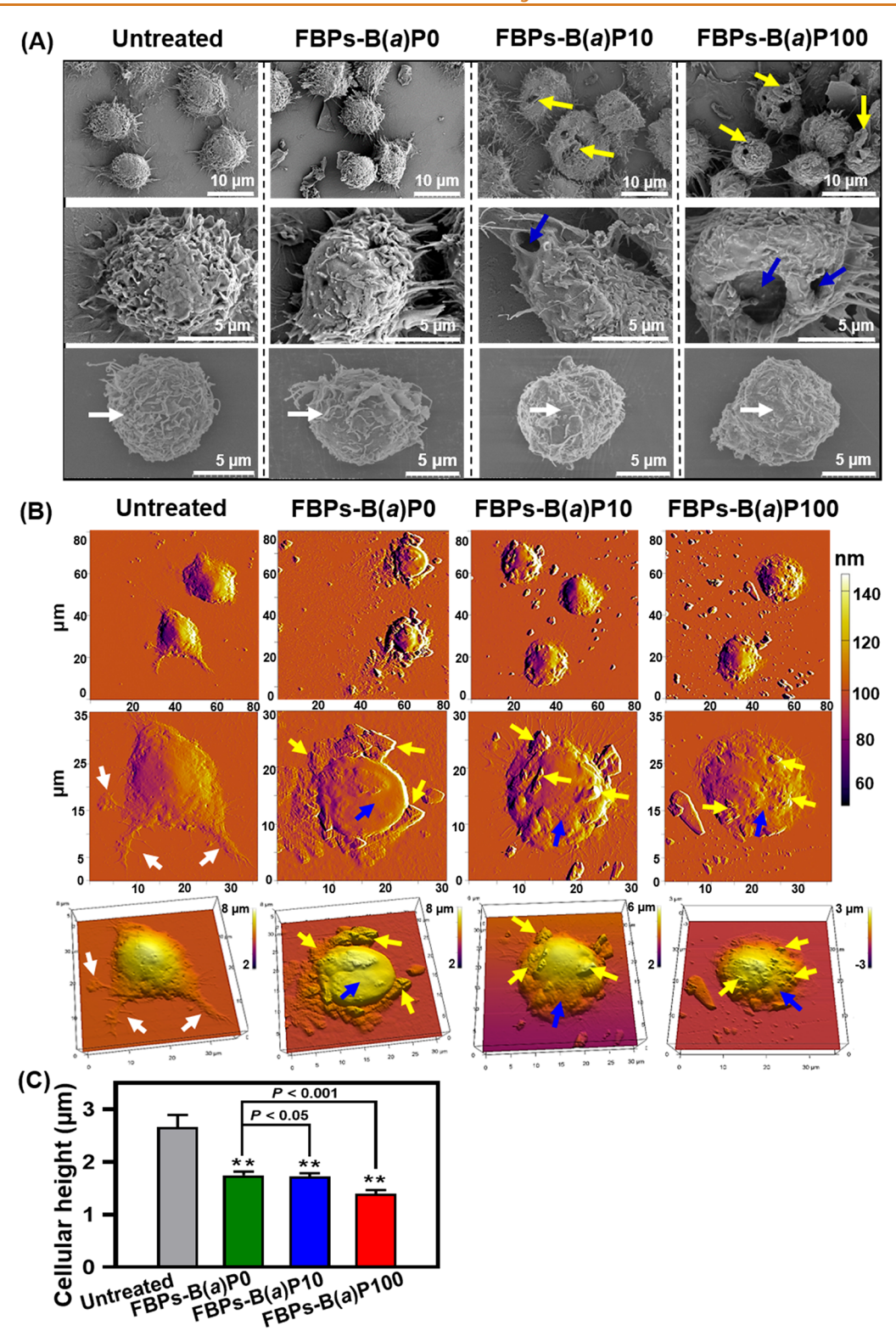


Figure 4. B(a)P-bearing FBPs caused morphological changes and plasma membrane damages. (a) Visualization of the interface between FBPs and cells determined by SEM. The upper panel represents low-magnification of SEM images of J774.A1 cells in response to pristine FBPs and B(a)P-bearing FBPs at 50  $\mu$ g/mL (determined by the mass concentration of FBPs) for 24 h, with enlarged images in the middle panel. Enlarged surface features of the individual cells are shown in the bottom panel (scale bar: 5  $\mu$ m). Yellow arrows denote the FBPs fusion or insertion into the plasma membrane. Blue arrows indicate the collapsed plasma membrane. White arrows point at the microvilli on the plasma membrane. (b) Visualization of the interplays between FBPs and cells using AFM. After 3 h of treatment with 10  $\mu$ g/mL FBPs, cells were fixed and imaged using AFM in a contact mode. Representative images of J774.A1 cellular topographies at different magnifications are shown. The 3D morphology images are shown in the bottom panel. Yellow arrows denote the FBPs. Blue arrows indicate the collapsed plasma membrane. White arrows point at the microvillus/pseudopodia on the plasma membrane. (c) Quantitative analysis of the cellular height changes in cells upon pristine FBP and B(a)P-bearing FBP treatment based on the high-resolution AFM topography data (n = 10).

3A). Additionally, as shown in Supplementary Figure 3B, incubation of the PAH-bearing FBPs (i.e., FBPs-B(a)P10, FBPs-B(a)P100, FBPs-Phe100, and FBPs-Pyr100) in full culture medium with 10% fetal bovine serum (FBS) for 24 h only resulted in limited PAH release (<10%), confirming the strong adsorption of PAHs to FBPs. The hydrodynamic diameter and surface charge of FBPs-B(a)P100 and FBPs-B(a)P10 were statistically indistinguishable from those of FBP-B(a)PO (Supplementary Figure 4A). The contact angle values of the B(a)P-bearing FBPs were slightly lower (P < 0.05), indicating that these particles might be more hydrophilic (which would promote particle dispersion). No statistical differences in the change of stability with time were observed among the three types of FBPs (Supplementary Figure 4B, P > 0.05). Additionally, the abundance of surface oxygen contents (represented by the O/C value) of B(a)P-bearing and B(a)Pfree FBPs were comparable (Supplementary Figure 4A) based on the X-ray photoelectron spectroscopy (XPS) (Supplementary Figure 4C) and Fourier transform infrared (FTIR) analyses (Supplementary Figure 4D), indicating that B(a)P adsorption had negligible effects on the surface oxygen functional groups of FBPs.

B(a)P-Bearing FBPs Incurred Greater Cell Death. Next, we examined the effects of B(a)P loading on the interactions of FBPs with susceptible cells, such as phagocytes.<sup>33</sup> Of note, the concentration of endotoxin in our FBPs was lower than the threshold of 0.25 EU/mL,<sup>34,35</sup> ruling out the disturbance of endotoxins. Here, as a widely used phagocyte model, J774.A1 macrophages were used. 36-38 As shown in Figure 2A, FBPs did not incur significant toxicity to J774.A1 cells with or without B(a)P binding at lower concentrations. However, a significant reduction in cell viability was observed in FBPs-treated cells at higher concentrations, such as 50 and 100  $\mu$ g/mL, especially at 100  $\mu$ g/mL (P < 0.05). Importantly, FBPs-B(a)P10 and FBPs-B(a)P100 showed greater toxicity in J774.A1 cells, in particular FBPs-B(a)P100, than that in FBPs-B(a)P0-treated cells. A similar trend was observed for FBPs-Wh, as B(a)P-loading FBPs-Wh also incurred a greater reduction of cell viability in J774.A1 cells (Figure 2B, P < 0.05). These results suggested that B(a)P adsorption caused greater cytotoxicity than the pristine FBPs. To tease out the source of toxicity, we further investigated whether the cytotoxicity probably was attributable to the dissolved free B(a)P. Notably, no observable decline was found in the cell viability of J774.A1 cells upon free B(a)Ptreatment at the concentrations from 1 to 50  $\mu$ g/L, which fully covered the concentrations of B(a)P with a maximum 10% dissolution percentage from FBPs-B(a)P10 and FBPs-B(a)-P100 in culture medium (Supplementary Figure 5), thus ruling out the contribution of dissolved free B(a)P to the overall toxicity of B(a)P-bearing FBPs in J774.A1 cells. Furthermore, the propidium iodide (PI) staining corroborated the greater cytotoxicity induced by FBPs-B(a)P10 and FBPs-B(a)P100 with 66% and 184% increase of PI-positive cells relative to FBPs-B(a)P0 treatment, respectively (Figure 2C,D, P < 0.001). We also carried out additional tests using FBPs-Phe and FBPs-Pyr and observed similar effects on cell viability (Supplementary Figure 6A,B) as that of B(a)P, indicating that other PAHs would exert similar effects on FBP toxicity to

As discussed above, we intentionally prepared the PAH-bearing and PAH-free FBPs using the same batch of materials with similar size and shape. In this premise, the observed changes in the toxicity of FBPs upon PAH loading should not

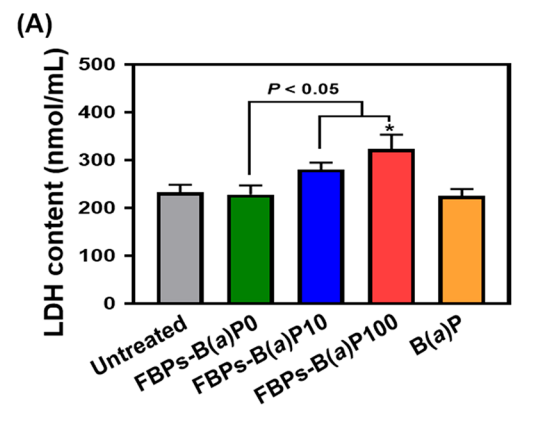
be ascribed to the results of altered particle size or morphology. Note that most of the previous studies on the toxic effects of PAHs on macrophages were carried out using exposure concentrations significantly higher than those in the environment, <sup>39–42</sup> whereas in this work, the majority of the PAHs was bound to the FBPs, and only a little PAHs were dissolved in the culture medium. Since no apparent toxic effects were observed at concentrations of freely dissolved B(a) P up to 50  $\mu$ g/L (Supplementary Figure 5), the observed cytotoxicity of PAH-bearing FBPs was unlikely caused by the B(a)P released from the FBPs. In the following, the particle bio interface between B(a)P-bearing FBPs and macrophages was comprehensively investigated. As shown in Figure 3A, massive FBPs were visualized to be associated with J774.A1 cells upon FBPs treatment for 24 h. The dramatic cellular morphological changes occurred in the phase-contrast images, as evidenced by the cellular size enlargement by 94% in FBPs-B(a)P100-treated cells relative to that of FBPs-B(a)P0-treated cells (Supplementary Figure 7, P < 0.001). Of note, even more severe insults were observed in cells upon treatment with FBPs-B(a)P100 than those in FBPs-B(a)P0, as cells exposed to FBPs-B(a)P100 displayed the most pronounced phenotypes with massive ingested FBPs inside the cells (Figure 3A, as denoted by yellow arrows, in the lower panel). To visualize and quantify the particle-bio interface in more detail, fluorescein isothiocyanate (FITC) conjugation, namely FITC-bovine serum albumin (BSA) to label particles dependent on the oxygen-containing functional groups was carried out to track particle uptake and localization through laser scanning confocal microscopy. This method was successfully used to qualitatively visualize and analyze the internalization of graphene oxide in macrophages in our recent work. 43,44 Here, our results showed that the attachment efficacy of FITC-BSA on FBPs was 49%, 43%, and 44% for FBPs-B(a)P0, FBPs-B(a)P10, and FBPs-B(a)P100, respectively, indicating that the fluorescent intensity for each FITC-conjugated FBPs was comparable.

As shown in Figure 3B, the mass of particles greatly differed inside the cells (as indicated by yellow arrows) and outside being attached to the plasma membrane (as denoted by white arrows) in pristine FBPs- and B(a)P-bearing FBPs-treated cells. After 6 h of incubation, only a small amount of FBPs-B(a)P0 could be observed inside cells, while a large amount of FITC-labeled FBPs-B(a)P10 and FBPs-B(a)P100 were accumulated in the cytoplasm (Figure 3B). In comparison to FBPs-B(a)P0-treated cells, the intercellular fluorescent intensity of FITC-labeled FBPs-B(a)P10 and FBPs-B(a)P100 was increased by 52% (P < 0.05) and 103% (Figure 3C, P < 0.001), respectively, highlighting that B(a)P adsorption reinforced the interaction between FBPs and plasma membrane and consequently induced a greater cellular engulfment of B(a)Pbearing FBPs. In support of these observations, the quantitative determination of cellular side scattering (SSC), an established flow cytometry method, based on the principle that the engulfed carbonaceous materials increase the cellular granularity, 45-47 unraveled an approximately 28% increase of FBPs in cells upon FBPs-B(a)P100, in comparison to cells exposed to FBPs-B(a)P0 (Supplementary Figure 8, P < 0.05).

Furthermore, SEM examination was performed to decipher the particle—membrane interplays in detail. As shown in Figure 4A, a distinct association of FBPs could be visualized upon treatment with B(a)P-bearing FBPs at 50  $\mu$ g/mL for 24 h, especially for FBPs-B(a)P100 (as denoted by yellow arrows, in the upper panel). As a result, incredible morphological

alterations occurred to the cells treated with B(a)P-bearing FBPs, as evidenced by plasma membrane collapse (as pointed at by blue arrows, in the middle panel) and shrunken surface microvilli (as pointed at by white arrows, in the bottom panel) (Figure 4A), compared to that of the untreated cells with typical cell spreading and microvilli. These impairments were even more severe in FBPs-B(a)P100-treated cells than those in cells treated with FBPs-B(a)P10, but these phenotypes could be hardly observed in FBPs-B(a)P0-treated cells and the untreated cells (Figure 4A). Additionally, we displayed the changes in cell morphology at the single-cell scale using an atomic force microscopy (AFM) platform, which is specialized in cell surface topography with the quantitative analysis of cellular height changes in response to particle interaction. <sup>48–50</sup> As shown in Figure 4B, FBPs-B(a)P10 and FBPs-B(a)P100 tended to penetrate and fuse with plasma membrane following incubation with cells at 10  $\mu$ g/mL for 3 h, especially the latter (as denoted by yellow arrows). FBP treatment altered the basic morphology of macrophages, as illustrated by the partial disappearance of microvillus/pseudopodia (as pointed at by white arrows). The three-dimensional (3D) topographies of cell membranes were also obtained using AFM, showing a much rougher and more uneven cell surface in FBPs-B(a)P10and FBPs-B(a)P100-treated cells than those observed in pristine FBPs-treated cells, in comparison to the untreated control cells (as pointed at by blue arrows, in the bottom panel of Figure 4B). To validate these findings, quantitative analysis of cellular height was implemented to evaluate morphological changes and plasma membrane damages responding to particle intrusion. As shown in Figure 4C, a significant reduction of cellular height was found in cells upon FBPs-B(a)P10 and FBPs-B(a)P100 treatment, especially the latter with 47% and 20% decrease relative to that of the control cells and FBPs-B(a)P0-treated cells, respectively (P < 0.001). Taken together, these results suggested that the intensive interactions between B(a)P-bearing FBPs and plasma membrane compromised the latter's integrity.

Next, to validate these findings, lactate dehydrogenase (LDH) release was carried out to evaluate cell membrane permeability. In parallel to the above cytotoxicity data, FBPs-B(a)P10 and FBPs-B(a)P100 caused the induction of LDH release approximately by 23% and 42% relative to FBPs-B(a)P0 treatment and the untreated control (Figure 5A, P <0.05). By contrast, no significant LDH induction was observed in FBPs-B(a)P0- and free B(a)P-treated cells (Figure 5A). To better shed light on the interactions between B(a)P-bearing FBPs and lipid membranes, we scrutinized the impact of B(a)P-bearing FBPs on the dynamic surface activity of Infasurf. Infasurf is a modified natural pulmonary surfactant extracted from the bronchoalveolar lavage of calves.<sup>38</sup> It is composed of mostly natural phospholipids with a small amount (~2 wt %) of hydrophobic surfactant associated proteins.<sup>51</sup> Pulmonary surfactant is synthesized by alveolartype II epithelial cells, and its main physiological function is to reduce the alveolar surface tension and to assist in innate immune defense against inhaled particles and pathogens.<sup>52</sup> We recently developed an in vitro experimental methodology called constrained drop surfactometry (CDS) in evaluating the pulmonary toxicity of carbonaceous nanomaterials and their adverse biophysical influence on pulmonary surfactant and other biomembranes. 53,54 We have demonstrated that Infasurf can be used in vitro as a model biomembrane to study the particle-bio interaction in the lung and at the surface of the



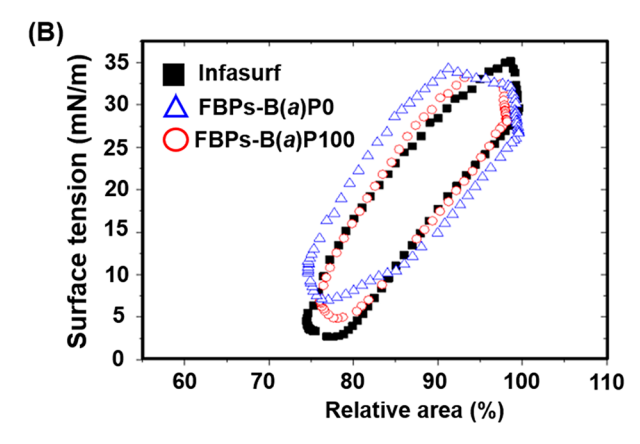


Figure 5. B(a)P-bearing FBPs incurred greater damages to the plasma membrane. (a) Quantification of LDH content in culture media from cells treated with pristine FBPs and B(a)P-bearing FBPs at 50  $\mu$ g/mL (determined by the mass concentration of FBPs) for 24 h (n=6). P<0.05 (\*) relative to the untreated control. Here,  $5\,\mu$ g/L B(a)P is accordingly used as the reference of maximum dissolved B(a)P. (b) CDS analysis of dynamic cycling of 1 mg/mL Infasurf (black square) exposed to FBPs-B(a)P0 (red circle) and FBPs-B(a)P100 (blue triangle) at 100  $\mu$ g/mL, respectively (determined by the mass concentration of FBPs). Each plot indicates a representative compression—expansion cycle of Infasurf with/without exposure to FBPs. The increase in the minimum surface tension at the end of compression indicates surfactant inhibition.

plasma membrane. 53-58 The biophysical impact of particles on pulmonary surfactants and biomembranes can be quantitatively determined with CDS through measuring the highly sensitive dynamic surface activity of Infasurf in response to the particles under physiologically relevant conditions. 54-58 As shown in Figure 5B, typical compression-expansion cycles of Infasurf were performed prior to the addition of 10 wt % FBPs. The dose of FBPs in the mixture of Infasurf and FBP solution corresponded to 100  $\mu$ g/mL, namely the highest FBP concentration tested in the cytotoxicity assays (Figure 2 and Supplementary Figure 6). It was found that FBPs-B(a)P100 induced more significant damage on Infasurf than FBPs-B(a)P0, indicated by the increase in the minimum surface tension  $(\gamma_{\min})$  at the end of film compression. Without these FBPs, Infasurf reached the  $\gamma_{min}$  of 2.5 mN/m with only 20% film compression (Figure 5B). The addition of FBPs-B(a)P0 and FBPs-B(a)P100 at 10 wt % increased the  $\gamma_{\min}$  to 4 and 7 mN/m, respectively, with the same 20% film compression. Increasing  $\gamma_{\min}$  upon exposure to particles is a strong indication of biophysical inhibition of the pulmonary surfactant, which

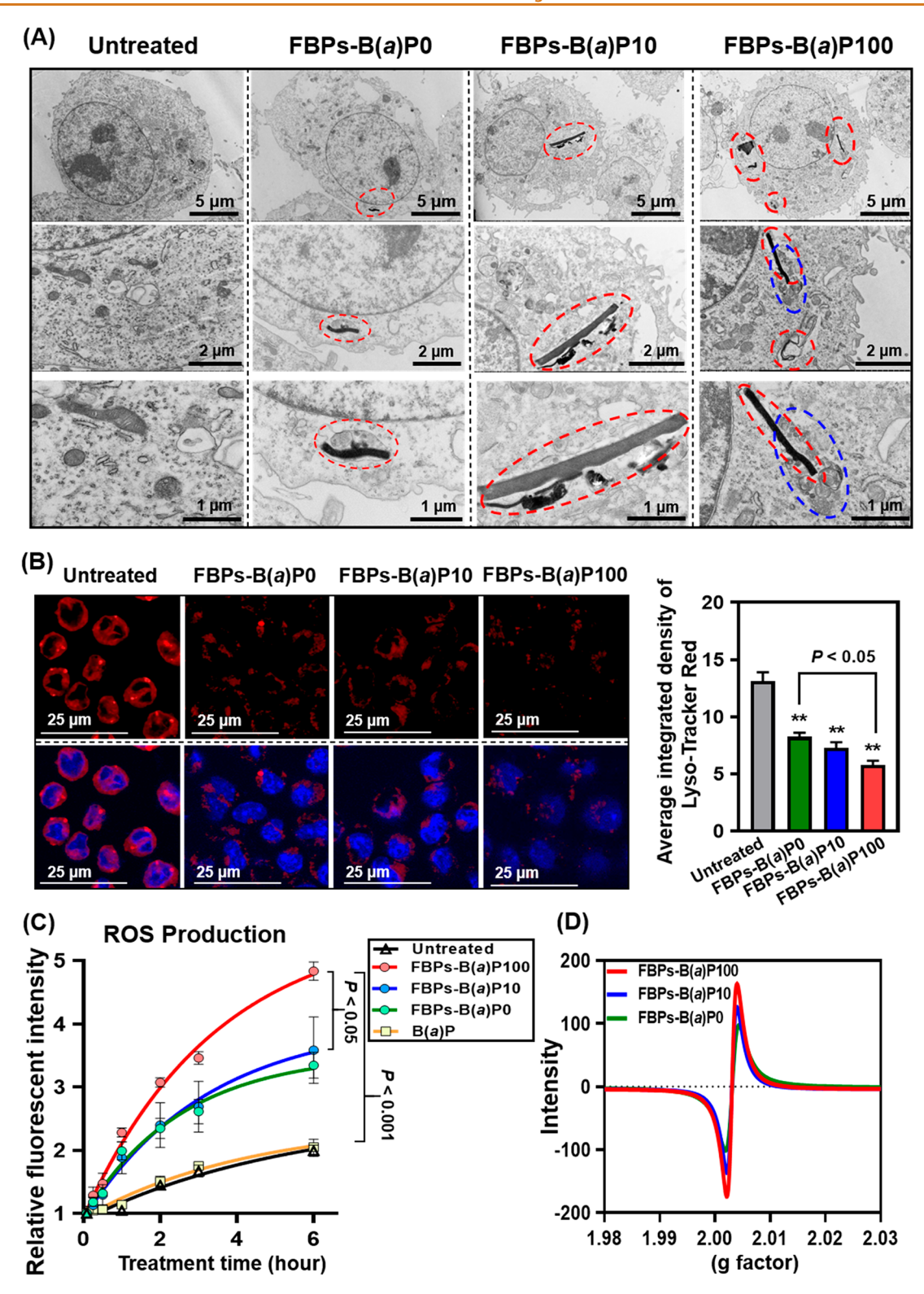


Figure 6. B(a)P-bearing FBPs resulted in elevated lysosomal injuries and oxidative stress in cells. (a) High-resolution TEM images displaying the intracellular localization of FBP sheets in J774.A1 cells upon pristine FBPs and B(a)P-bearing FBPs at  $10 \mu g/mL$  (determined by the mass concentration of FBPs) for 24 h. The red circles denote the intracellular engulfed FBPs, and the blue circles indicate the autophagosome-like structure. (b) Fluorescent images of J774.A1 cells stained with Lyso-Tracker Red DND-99 (red, in the upper panel) and Hochest33342 (blue, merged images are shown in the lower panel) following treatment with 50  $\mu g/mL$  pristine FBPs and B(a)P-bearing FBPs (determined by the mass concentration of FBPs) for 24 h. The quantitative analysis of Lyso-Tracker Red staining using the ImageJ software is shown in the right panel. P < 0.001 (\*\*) relative to the untreated control. (c) Quantification of ROS production in response to 50  $\mu g/mL$  pristine FBPs and B(a)P-bearing FBPs (determined by the mass concentration of FBPs) at different time points (n = 6). Here, 5  $\mu g/L$  E(a)P is accordingly used as the control of maximum dissolved E(a)P. (d) EPFR spectra monitored for pristine FBPs and E(a)P-bearing FBPs.

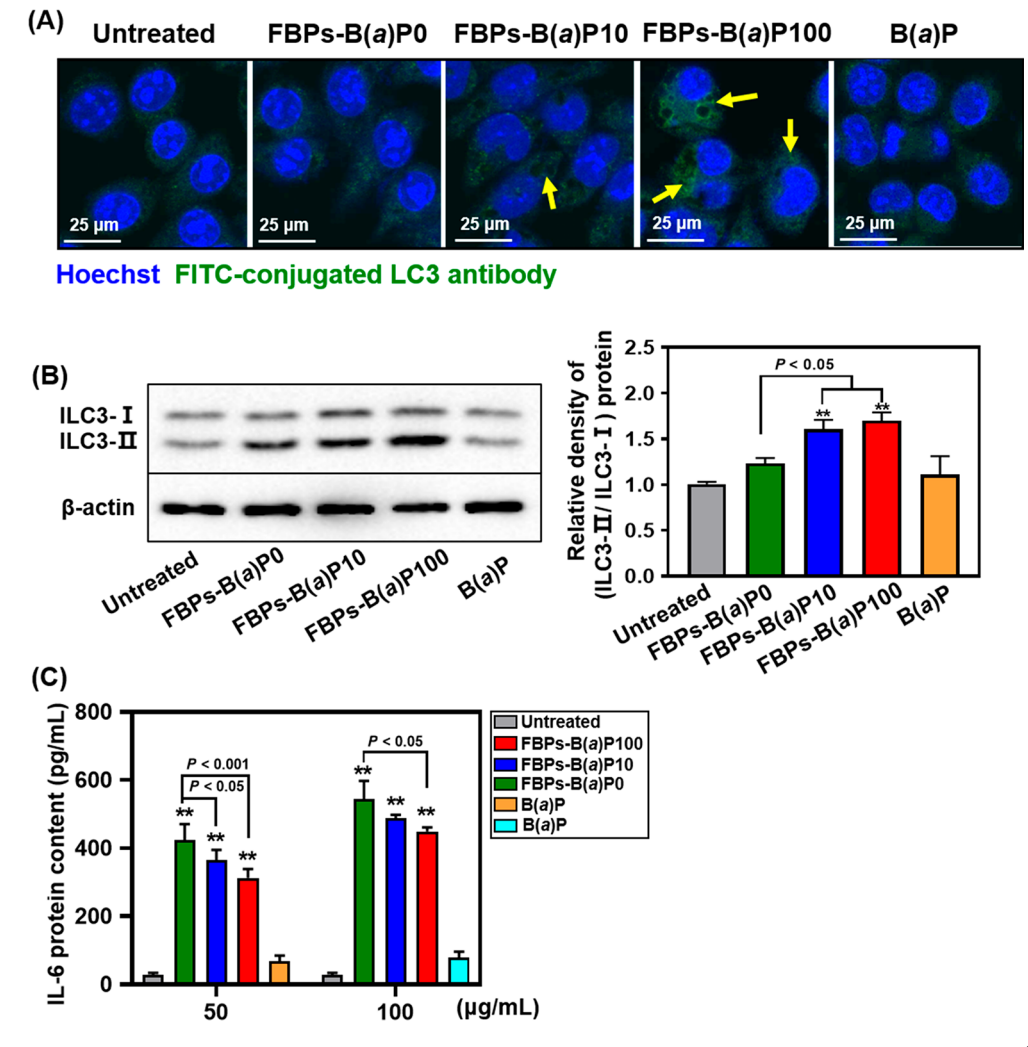


Figure 7. B(a)P-bearing FBPs incurred greater autophagy and compromised proinflammatory reactions in macrophages. (a) Representative immunofluorescent images with the accumulation of green fluorescent puncta in J774.A1 cells responding to pristine FBPs and B(a)P-bearing FBPs (determined by the mass concentration of FBPs) at 50  $\mu$ g/mL for 48 h. FITC-conjugated LC3 signal (green) and Hochest 33342 signal (blue) are merged. Here, 5  $\mu$ g/L B(a)P is applied as the control of freed B(a)P. The yellow arrows denote the formed autophagosomes with FITC-containing puncta. (b) Western blotting analysis of the conversion of LC3 from LC3-I to LC3-II in macrophages upon pristine FBPs and B(a)P-bearing FBPs (determined by the mass concentration of FBPs) at 50  $\mu$ g/mL for 48 h. Here, 5  $\mu$ g/L B(a)P was applied as the control of freed B(a)P. Quantitative data are shown in the right panel (n = 4). P < 0.001 (\*\*) relative to the untreated control. (c) The protein concentration of IL-6 in culture media collected from J774.A1 cells treated with 50 and 100  $\mu$ g/mL pristine FBPs and B(a)P-bearing FBPs (determined by the mass concentration of FBPs) for 24 h (n = 4). Here, 5 and 10  $\mu$ g/L B(a)P was used as the reference of maximum dissolved B(a)P from FBPs at 50 and 100  $\mu$ g/mL, respectively.

can be caused by disturbance of the phospholipid molecular conformation, phase behavior, and/or denaturation of surfactant-associated proteins.<sup>59</sup> Therefore, it can be inferred that the B(a)P-bearing FBPs were more potent to disturb the dynamic structure of phospholipid membranes than the pristine FBPs. It has been demonstrated that hydrophobic particles were more readily trapped by pulmonary surfactant films, while hydrophilic particles quickly penetrated the surfactant monolayer. <sup>60,61</sup> Hydrophobic particles also harbored a higher tendency to directly interact with both lipid and protein components in pulmonary surfactant to form a lipoprotein biomolecular corona. 62 In addition, it has been reported that perfluorocarbon gases and other volatile organic compounds (i.e., benzene, toluene, ethylbenzene, and p-xylene) with low polarity can significantly increase  $\gamma_{\min}$  of pulmonary surfactant, likely by penetrating the surfactant film and thus directly disturbing the lipid ordering. 63,64 B(a)P is a small

hydrophobic molecule that contains five benzene rings (Supplementary Figure 2). During the compression-expansion cycle conducted by CDS, the surfactant lipids and/or proteins could get in and out of the pores in FBPs and thus gain direct contact with B(a)P trapped inside the pores. These B(a)P molecules trapped in FBPs would be difficult to dissolve upon contact with the lipid-enriched pulmonary surfactants and cell membrane (Supplementary Figure 3A,B), thus disturbing and fluidizing the biomembranes by directly inserting into the lipid membranes. Such an effect may be comparable to the inhibitory effect on the membrane fluidization caused by cholesterol and free fatty acids that disturb biomembranes by penetrating and intercalating lipid molecules. 65,66 Although direct evidence along this direction is still yet to be developed, our forementioned data uncovered that more particle internalization was observed in cells treated with FBPs-B(a)P100, most likely owing to a direct result of membrane fluidization and disturbance (Figures 3 and 4). To this end, these findings together uncovered that the particle—bio interactions would be greatly disrupted upon B(a)P-bearing FBPs.

B(a)P-Bearing FBPs Resulted in Elevated Lysosomal Injuries and Oxidative Stress in Cells. The above findings on the enhanced phospholipid film injuries and cellular uptake of B(a)P-bearing FBPs would entail carefully examining the subcellular localization of FBPs in more details. As shown in Figure 6A, the ultrastructural images assessed by transmission electron microscope (TEM) identified the intracellular localization of FBPs (denoted by red circles), most likely within the fusion body formed by lysosome and phagosome (the enlarged images were shown in the middle and bottom panels). Consistently, greater accumulation was observed in cells in response to FBPs-B(a)P100 and FBPs-B(a)P10, compared to cells upon FBPs-B(a)P0 (Figure 6A). In agreement with previous reports, <sup>67,68</sup> in a consequence, enhanced endocytosis and the fusion between lysosomes and phagosomes incurred injuries of the phagolysosomes and lysosomes in cells treated with FBPs, compared to the untreated cells, as reflected by the broken lysosomes visualized by the Lyso-Tracker Red DND-99 dye (Figure 6B, P < 0.05). To a greater extent, FBPs-B(a)P100 caused more reduction of lysosomal staining relative to that upon FBPs-B(a)P0 treatment (Figure 6B, P < 0.05).

In the meantime, intracellular reactive oxygen species (ROS) production was also boosted in FBP-treated cells in comparison to the untreated control and free B(a)P-treated cells (Figure 6C, P < 0.05). Of note, in agreement with the most significant cellular endocytosis and cytotoxicity, the greatest ROS induction was found in cells upon FBPs-B(a)P100 (Figure 6C, P < 0.001). For example, a 150% increase of ROS production was demonstrated in FBPs-B(a)P100-treated cells at 50  $\mu$ g/mL for 6 h, whereas 80% and 67% increase were found in FBPs-B(a)P10- and FBPs-B(a)P0treated cells, compared to the untreated cells and free B(a)Ptreated cells (Figure 6C, P < 0.001). To exclude the likely contribution of dissolved B(a)P to the overall ROS generation, free B(a)P at a wide range of concentrations, covering the maximum dissolution from the B(a)P-bearing FBPs, was used in the ROS generation assay. As shown in Supplementary Figure 9, no ROS was kindled in J774.A1 cells upon B(a)P at various concentrations, excluding the contribution of dissolved B(a)P to the overall ROS production in B(a)P-bearing FBPstreated cells. The g-factor, suggestive of the environmentally persistent free radical (EPFR) type, <sup>69,70</sup> was constant as 2.003 for pristine FBPs and B(a)P-bearing FBPs (Figure 6D), indicating that the EPFR of FBPs was carbon centered with an adjacent oxygen atom,  $^{71}$  and B(a)P loading did not alter the EPFR type of FBPs. Together, these results unearthed more active changes of B(a)P-bearing FBPs in penetrating the cells, incurring lysosomal damage and inducing oxidative stress in comparison to that of pristine FBPs.

**B**(a)P-Bearing FBPs Incurred Greater Autophagy and Compromised Proinflammatory Reactions in Macrophages. Phagolysosome and lysosomal damages are often linked to autophagy,<sup>72</sup> a type of cell death with unique features and displays, such as the formation of autophagosomes.<sup>73</sup> As described above in Figure 6A, our data suggested the formation of autophagosomes in cells upon FBPs-B(a)P (as denoted by blue circles), hinting the occurrence of autophagy in FBPs-B(a)P-treated cells. To address this likelihood, the formation of autophagosome was assessed through visualizing the

transformation of cytoplasmic LC3 into accumulated LC3 puncta using a FITC-conjugated LC3 antibody (Ab).<sup>72</sup> As shown in Figure 7A, representative autophagosomes were visualized in J774.A1 cells upon FBPs-B(a)P10 and FBPs-B(a)P100, in particular the latter, as characterized by the formation of LC3 puncta in a round shape with stronger fluorescence (Figure 7A, as indicated by yellow arrows). Quantitative analysis of fluorescence intensity revealed a 34% and 80% increase in J774.A1 cells upon FBPs-B(a)P10 and FBPs-B(a)P100, respectively, compared to that in FBPs-B(a)P0-treated cells (Supplementary Figure 10, P < 0.05), highlighting the formation of autophagosomes. In support of this finding, the increased conversion of LC3-I to LC3-II, a hallmark of autophagosome accumulation, <sup>74</sup> was found in cells treated with FBPs-B(a)P10 and FBPs-B(a)P100, in particular the latter, compared to the untreated cells and cells treated with FBPs-B(a)P0, as determined by Western blotting analysis (Figure 7B). Quantified data of multiple biological replicates unraveled that 70% and 38% elevation of the relative ratio of LC3-II to LC3-I in FBPs-B(a)P100-treated cells, compared to that in the untreated cells and FBPs-B(a)P10-treated cells, respectively (Figure 7B, P < 0.05, in the right panel). In agreement with our above results, free B(a)P did not elicit the activation of autophagosomes in macrophages (Figure 7A,B), ruling out the implication of free B(a)P in triggering autophagy. Additionally, the functionality of macrophages was assessed post-B(a)P-bearing FBP treatment. Consistent with our recent studies on the proinflammatory reactions upon carbonaceous particles in macrophages, 75,76 our pristine FBPs, namely FBPs-B(a)P0, largely provoked the proinflammatory reactions, as reflected by the induction of interleukin 6 (IL-6) (Figure 7C, P < 0.001). However, compromised production of IL-6 cytokine was found in cells upon FBPs-B(a)P10 and FBPs-B(a)P100, especially the latter, relative to FBPs-B(a)P0, at both 50  $\mu$ g/mL and 100  $\mu$ g/mL (Figure 7C, P < 0.05), indicating blunted proinflammatory responses in FBPs-B(a)Ptreated cells. Supported by another proinflammatory cytokine, tumor necrosis factor  $\alpha$  (TNF- $\alpha$ ), diminished expression was also observed in FBPs-B(a)P10- and FBPs-B(a)P100-treated cells, compared to cells upon FBPs-B(a)P0, and FBPs-B(a)P100 caused a greater inhibition on TNF- $\alpha$  gene expression than FBPs-B(a)P10 (Supplementary Figure 11, P < 0.05). In our study, B(a)P also did not prime the proinflammatory status of macrophages (Figure 7C and Supplementary Figure 10). Analogously, this descending trend was also corroborated by the data of IL-6 production in J774.A1 cells responding to other PAH-bearing FBPs, including FBPs-Wh-B(a)P (Supplementary Figure 12, P < 0.05), FBPs-Phe, and FBPs-Pyr (Supplementary Figure 13, P < 0.05). These collective data unveiled that PAH-bearing FBPs induced autophagy and undermined the innate immune defense (e.g. the proinflammatory reactions) in macrophages.

# **CONCLUSIONS**

In this study, we found that the binding of PAHs at environmentally relevant exposure concentrations to FBPs greatly affected the toxicological effects of the particles, by enhancing the interactions between the particles and the target cells. These findings unravel a previously unrecognized toxicity mechanism for contaminant-bearing PMs. Thereby, in addition to the previously identified "Trojan-horse" effect (namely, the vehicle-aided transportation of organic pollutants by PMs), the PM-associated contaminants appear to play an active role in

the joint toxicity of contaminant PM complex by altering the bioreactivity of PMs, leading to an enhanced disruption of phospholipid membrane, endocytosis, oxidative stress, autophagy, and otherwise compromised immune responses in macrophages, compared to those of contaminant-free PMs. It is noteworthy that this mechanism may not be limited to FBPs only, but also viable for other types of carbonaceous particles, even though the specific effects may likely be particle dependent, determined by a range of different physicochemical properties of the particles of concern. Under this context, more studies are needed to precisely understand the effects of contaminant binding on particle-bio interactions. Moreover, besides PAH accumulation during biomass pyrolysis, sources of FBP-bearing contaminants also include contaminant adsorption from the aqueous solutions (e.g., during biochar application as sorbents to sequester environmental contaminants). Contaminants accumulation from these other sources may involve different contaminant-biochar interactions (e.g., slow diffusion of dissolved molecules in micropores of FBPs). Future studies thereby should fully consider the effects of such dynamic processes on the interplay between contaminants and FBPs and the associated joint toxicity. Overall, our findings highlight the importance of understanding the interfacial chemical behaviors of different chemical components in PMs, as such interactions may significantly affect the bioactivity of PMs and, consequently, the toxicity profiles.

# **EXPERIMENTAL SECTION**

**Preparation of FBPs and PAH-Bearing FBPs.** The FBPs were produced from corn straw and wheat stalk under 500 °C and oxygen-limited conditions using a box-type atmosphere furnace (Action machinery manufacturing, Shanghai, China). The particles were crushed in ultrapure water (BeyoPure, Shanghai, China), passed through a 3  $\mu$ m sieve, and then settled for 24 h to remove large particles. Then the raw FBPs were collected by filtering the suspension through a 0.22  $\mu$ m polyether sulfone membrane. The collected FBPs were subsequently washed with ultrapure water for 3 times to remove the foam and then subjected to vacuum freeze-dry to obtain the ideal biochar powder. The <sup>14</sup>C- labeled B(a)P (26.6 mCi/mmol), <sup>14</sup>C- labeled Phe (55 mCi/mmol), and <sup>14</sup>C- labeled Pyr (58.8 mCi/mmol) were purchased from the American Radiolabeled Chemicals (St. Louis, MO), and nonlabeled PAHs were purchased from the Sigma-Aldrich Chemicals (St. Louis, MO).

The PAH-bearing FBPs were prepared using the reported method.  $^{19-21,23}$  Briefly, 0.1 g of clean FBPs and 0, 10, or 100  $\mu g$  of <sup>14</sup>C-labeled PAHs or nonlabeled PAHs were suspended in 20 mL of acetone solution and incubated in an ultrasonic bath at room temperature for 1 h. After subsequent vacuum desiccation, the control sample (FBPs without PAH loading, named as FBPs-B(a)P/Phe/ Pyr0) and samples loaded with 10 or 100  $\mu$ g/g of PAH named as FBPs-B(a)P/Phe/Pyr10, FBPs-Wh-B(a)P10, FBPs-B(a)P/Phe/ Pyr100, and FBPs-Wh-B(a)P100, respectively, were stored at room temperature. The loading efficacy of PAHs on FBPs was measured as follows: After the combustion of 14C-PAH-bound FBPs at 800 °C with a biological oxidizer (OX-500, Zinsser Analytic, Germany), the generated <sup>14</sup>CO<sub>2</sub> was collected using alkaline cocktail Oxysolve C-400 (Zinsser Analytic, Germany), and the content of collected 14CO2 was counted using a liquid scintillation counter (LS6500, Beckman Coulter, Brea, CA). The loading efficacies of PAHs were subsequently accessed by calculating the radioactivity of recovered 14CO2 to the total spiked amount based on the equation:  $F_e = R_r/R_s \times 100$ , where  $F_{\rm e}$  was the loading efficacy (%),  $R_{\rm r}$  indicated radioactivity of recovered  $^{14}\mathrm{CO}_2$ , and  $R_\mathrm{s}$  represented the total spiked  $^{14}\mathrm{C}$  in form of PAHs. The dissolution efficacy of PAHs from FBPs in culture medium was determined using our established approach, as described.<sup>2</sup>

Characterization of Physicochemical Properties of FBPs and PAH-Bearing FBPs. The morphological properties of FBPs were characterized by SEM (Hitachi S-3400 N II, Japan), and the size distribution of FBPs was assessed using the ImageJ software (NIH, USA, http://rsbweb.nih.gov) by measuring more than 200 particles in SEM images. The surface area and micropore volume of FBPs were determined by the N2 adsorption/desorption at 77 K using an accelerated surface area and porosimetry system (Micromeritics ASAP 2460, Norcross, GA). Surface area was calculated by the Brunauer-Emmett-Teller method, and the specific external and micropore surface area were obtained by the t-plot method. Volume and average diameter of micropore and mesopore were obtained from desorption isotherms using the Horvath-Kavazoe and the Barrett-Joyner-Halenda methods, respectively. Contact angles, hydrodynamic diameter, and  $\zeta$ -potential of FBPs in culture medium were measured using OCA-20 contact angle system (Dataphysics, Germany), laser particle size analyzer (Beckman Coulter LS13 320, Irvine, CA), and particle analyzer (Anton Paar Litesizer 500, Graz, Austria), respectively. The EPFR spectra were determined on an electron paramagnetic resonance spectrometer (Bruker EMX Plus 6-1, Germany). The FTIR spectrum was implemented from 4000 to 400 cm<sup>-1</sup> on a FTIR spectroscopy (Spectrum One, PerkinElmer Instruments Co. Ltd. USA) to identify the presence of functional groups in FBPs. The O/C value was afterward measured based on XPS (PHI 5000 VersaProbe, Ulvac-Phi, Japan) and FTIR analyses. The endotoxin level was determined using a Limulus Amebocyte Lysate (LAL) kit (Pierce, USA).

Cell Culture and Cell Viability Assessment. Murine macrophage cell line J774.A1 was purchased from the Shanghai Cell Bank of Type Culture Collection at the Chinese Academy of Sciences. J774.A1 cells were cultured in Dulbecco's modified Eagle's medium (Gibco life technology, USA) at 37 °C with 5% CO $_2$ , supplemented with 10% FBS and 100 U/mL of penicillin/streptomycin. Cell viability was assayed with a live/dead viability/cytotoxicity kit (Invitrogen Inc., USA) according to the manufacturer's instructions. Cellular areas were measured and calculated by ImageJ software. Cell death was determined by PI staining. In brief, cells were stained with PI dye (5  $\mu$ L per 1  $\times$  10 $^5$  cells at 4 °C for 30 min) after treatment. The stained cells were visualized on a fluorescence microscope (Axioscope A1, ZEISS). $^{77}$ 

**Assessment of Cellular ROS.** For the analysis of ROS production, cells were collected and washed after treatment. Thereafter, 5  $\mu$ M dichlorofluorescein-diacetate (DCF-DA, Sigma, MO, USA) was applied to incubate with cells in 100  $\mu$ L of phosphate buffer saline (PBS, Solarbio, Inc., Beijing, China) for 30 min at 37 °C. After washing with PBS for 3 times thoroughly to clean the unabsorbed DCF-DA probe, the intensity of the DCF fluorescence was thereafter recorded at 525 nm on a plate reader (Thermo Fisher Scientific Inc., USA) using the excitation wavelength of 488 nm at the corresponding time points, as described. <sup>76</sup>

Characterization of the Phagosome and Autophagosome. The phagosomes were examined by TEM. Briefly, cells were washed and collected gently post-treatment, and cells were then subjected to fixing with 2.5% glutaraldehyde solution, followed by embedding with epoxy resin. Ultrathin sections (70 nm) were stained with 1% lead citrate and 0.5% uranyl acetate, followed by examination on a high-resolution TEM (JEOL JEM 2010F, Hitachi Scientific Instruments, Japan).

Autophagosome characterization was also performed through confocal laser scanning microscopy dependent on the immunofluor-escence of FITC-labeled LC3 protein. Following treatment, cells were washed twice with cold PBS and were fixed with cold methanol for 15 min at  $-20\,^{\circ}\text{C}$ . In the following, cells were washed with PBS for 5 min and 3 times. After blocking in blocking buffer (PBS containing 5% goat serum and 0.3% Triton X-100) for 1 h, cell specimens were subjected to the incubation with the primary Ab (LC3B (D11) XP@ rabbit mAb, Cell Signaling Technology, 1:1,000) overnight at 4 °C. Following rinsing 3 times in PBS each for 5 min, cells were incubated with FITC-conjugated secondary Ab (anti-rabbit IgG, F(ab')2 fragment, Cell Signaling Technology, 1:5000) for 2 h at room

temperature in the dark. Finally, nuclei were stained with 1  $\mu$ g/mL Hoechst 33342 dilution (Trihydrochloride, Thermo Fisher Inc., USA) for 20 min and were then protected with an antifluorescent quenching agent (Solarbio) for further examination.

**Evaluation of Lysosomal Damage.** To visualize the damage of the lysosome, the staining of the lysosome was performed using a fluorescent acidotropic probe, LysoTracker. Cells were incubated for 1 h with 50 nM Lyso-Tracker Red (Thermo Fisher), and the staining solution was then replaced with fresh medium containing Hoechst 33342 dilution to counter nuclei. The integrated intensity of Lyso-Tracker Red was quantitatively calculated based on the equation: integrated intensity = area × mean (the area and mean for each cell were determined by the Image] software).

**Analysis of Intracellular FBPs.** The intracellular location of FBPs was examined in the TEM images. To quantify the cellular uptake of FBPs, we used an established flow cytometry technology based on the principle that the engulfed particles increase the cellular granularity of cells, as evidenced by the quantitative increase in cellular SSC. <sup>45–47</sup> Cells were gently collected, and the changes of SSC were assessed according to the SSC values by flow cytometry.

Characterization of FBP–Membrane Interaction. For the visualization of interaction between cells and FBPs, FITC-BSA was labeled on FBPs following an established method. The fluorescence intensity and the concentration of FITC-BSA conjugated to FBPs were determined through an ultramicrofluorescence spectrophotometer (DS-11FX+, DeNovix Inc., USA). The integrated intensity of intracellular FITC-labeled FBPs was quantitatively calculated with the ImageJ software. For the analysis of cell morphology changes in response to FBP interaction, fixed cells were subjected to the imaging using AFM platform (MFP-3D Infinity, Oxford Instruments, Inc., UK).

Determination of Inflammatory Cytokines. Cells were seeded in 96-well plates (Corning Inc., USA) overnight and were then treated with FBPs and B(a)P-bearing FBPs at various concentrations. Afterward, the concentration of IL-6 cytokine in the culture media was determined with an ELISA kit according to the manufacturer's instructions (NeoBioscience Inc., Shenzhen, China). Meanwhile, reverse transcription and quantitative polymerase chain reaction (RTqPCR) were carried out for the analysis of the mRNA transcript expression of TNF- $\alpha$ . Briefly, cells were cultured in 12-well plates, followed by different treatments. Afterward, Trizol reagent (Invitrogen) and MonScript RTIII (Monad Inc., Beijing, China) were used for RNA extraction and cDNA synthesis, respectively. qRT-PCR analysis of TNF-\alpha gene expression (forward primer: 5'-GACGTG-GAACTGGCAGAAGAGG-3; reverse primer: 5'-TGACGGCGA-GAGGAGGTTGAC-3') was determined using SYBR Green qPCR Mix (Promega Inc., USA) on an Mx3005P qRT-PCR instrument (Bio-Rad, USA). Hypoxanthine phosphoribosyitransferase 1 was used as the loading control for normalization (forward primer: 5'-GCTTGCTGGTGAAAAGGACCTCTCGAAG-3'; reverse 5'-CCCTGAAGTACTCATTATAGTCAAGGGCAT-3').

Western Blotting Analysis. Post-treatments, cells were collected and lysed in RIPA lysate buffer (Solarbio) containing the protease inhibitor cocktail (Roche Inc., Switzerland). The concentrations of extracted total proteins were determined with the BCA method according to the instructions from the manufacturer (Solarbio). Afterward, Western blot analysis was carried out with an antimouse LC3 Ab (1:1000, Abcam, Biotechnology Inc.) and antimouse  $\beta$ -actin Ab (1:5,000, Proteintech Group Inc., USA, used as a loading control). The intensity for autoradiogram in Western blots was quantified using the ImageJ software, and the intensity of each band was normalized to that of  $\beta$ -actin.

Detection of the Interaction between FBPs and Plasma Membrane by SEM and CDS Platform. For topographical analysis of cell membrane upon FBP exposure, harvested cells were fixed with 2.5% glutaraldehyde solution and were then challenged with desiccation and spray-gold. The association of FBPs and the cellular topography were examined by a SEM (JSM-6400, JEOL Lim. Co., Japan).

To quantitatively evaluate the damage of FBPs on a model biomembrane, the CDS was used to assess the dynamic surface activity of an animal-derived natural pulmonary surfactant, Infasurf (ONY Biotech, NY, USA), with or without exposure to FBPs. CDS is an established surface tensiometry technique used to study the effect of particles on biomembrane under physiologically and pathologically relevant conditions. <sup>53,54</sup> Briefly, the mix of FBPs and Infasurf at a mass ratio of 10% was incubated at 37 °C for 1 h before the CDS measurement. After adsorption, the surfactant film was compressed and expanded at a rate of 3 s per cycle with a compression ratio controlled at no more than 25% of the initial surface area to simulate normal tidal breathing. Biophysical properties were examined from the resulted dynamic surface tension—surface area loops. The experimental conditions were controlled at 37 °C and with 100% relative humidity to mimic the intra-alveolar environment.

**LDH Release Assay.** For the cell membrane permeability assay, the amount of LDH released in culture media after treatments was determined using an LDH Assay (Jiancheng, Inc., Nanjing, China).

**Statistical Analysis.** An independent *t*-test with the SPSS software was used to analyze the experimental data. Experimental data are shown in mean  $\pm$  standard deviation. Statistical significance was determined with P < 0.05 and P < 0.001.

## **ASSOCIATED CONTENT**

# Supporting Information

The Supporting Information is available free of charge at https://pubs.acs.org/doi/10.1021/acsnano.1c00324.

Supplementary results about physicochemical properties of PAH-bearing FBPs, assessment of cell viability and cellular ROS production, detection of autophagosome, and determination of inflammatory cytokines (PDF)

# **AUTHOR INFORMATION**

# **Corresponding Authors**

Wei Chen — College of Environmental Science and Engineering, Ministry of Education Key Laboratory of Pollution Processes and Environmental Criteria, Tianjin Key Laboratory of Environmental Remediation and Pollution Control, Nankai University, Tianjin 300350, China;
orcid.org/0000-0003-2106-4284; Email: chenwei@nankai.edu.cn

Sijin Liu – State Key Laboratory of Environmental Chemistry and Ecotoxicology, Research Center for Eco-Environmental Sciences, Chinese Academy of Sciences, Beijing 100085, China; School of Environmental Sciences, University of Chinese Academy of Sciences, Beijing 100049, China; orcid.org/0000-0002-5643-0734; Email: sjliu@rcees.ac.cn

### **Authors**

Juan Ma – State Key Laboratory of Environmental Chemistry and Ecotoxicology, Research Center for Eco-Environmental Sciences, Chinese Academy of Sciences, Beijing 100085, China; School of Environmental Sciences, University of Chinese Academy of Sciences, Beijing 100049, China

Xinlei Liu — College of Environmental Science and Engineering, Ministry of Education Key Laboratory of Pollution Processes and Environmental Criteria, Tianjin Key Laboratory of Environmental Remediation and Pollution Control, Nankai University, Tianjin 300350, China

Yi Yang — Department of Mechanical Engineering, University of Hawaii at Manoa, Honolulu, Hawaii 96822, United States

Jiahuang Qiu — State Key Laboratory of Environmental Chemistry and Ecotoxicology, Research Center for Eco-

- Environmental Sciences, Chinese Academy of Sciences, Beijing 100085, China; School of Environmental Sciences, University of Chinese Academy of Sciences, Beijing 100049, China
- Zheng Dong State Key Laboratory of Environmental Chemistry and Ecotoxicology, Research Center for Eco-Environmental Sciences, Chinese Academy of Sciences, Beijing 100085, China; School of Environmental Sciences, University of Chinese Academy of Sciences, Beijing 100049, China
- Quanzhong Ren State Key Laboratory of Environmental Chemistry and Ecotoxicology, Research Center for Eco-Environmental Sciences, Chinese Academy of Sciences, Beijing 100085, China; School of Environmental Sciences, University of Chinese Academy of Sciences, Beijing 100049, China
- Yi Y. Zuo Department of Mechanical Engineering, University of Hawaii at Manoa, Honolulu, Hawaii 96822, United States; orcid.org/0000-0002-3992-3238
- Tian Xia Center of Environmental Implications of Nanotechnology (UC CEIN), California NanoSystems Institute, and Division of NanoMedicine, Department of Medicine, University of California, Los Angeles, California 90095, United States; orcid.org/0000-0003-0123-1305

Complete contact information is available at: https://pubs.acs.org/10.1021/acsnano.1c00324

# **Author Contributions**

"These authors equally contribute to this work. W.C. and S.L. conceived and designed the study. J.M. carried out cell experiments with the help of Z.D., J.Q., and Q.R. X.L. prepared the FBPs and analyzed their physicochemical properties. The manuscript was written through contributions from all authors. All authors approved the final version of the manuscript.

# Notes

The authors declare no competing financial interest.

# **ACKNOWLEDGMENTS**

This work was supported by grants from the National Natural Science Foundation of China (grant numbers: 22076210, 21707161, and 21920102007), the National Key Research and Development Program of China (grant number: 2018YFA0901101), an International Collaboration Key Grant from the Chinese Academy of Sciences (grant number: 121311KYSB20190010), and the Beijing Natural Science Foundation (grant number: 8191002). We thank Dr. Rong Ji, School of the Environment, Nanjing University, China, for generously providing <sup>14</sup>C-labeled PAHs and guiding relative experiments. We thank all the laboratory members for their assistance with experiments and reagents.

# **REFERENCES**

- (1) Lu, S.; Zong, Y. Pore Structure and Environmental Serves of Biochars Derived from Different Feedstocks and Pyrolysis Conditions. *Environ. Sci. Pollut. Res.* **2018**, 25 (30), 30401–30409.
- (2) Sigmund, G.; Jiang, C. J.; Hofmann, T.; Chen, W. Environmental Transformation of Natural and Engineered Carbon Nanoparticles and Implications for the Fate of Organic Contaminants. *Environ. Sci.: Nano* **2018**, *5* (11), 2500–2518.
- (3) Spokas, K. A.; Novak, J. M.; Masiello, C. A.; Johnson, M. G.; Colosky, E. C.; Ippolito, J. A.; Trigo, C. Physical Disintegration of Biochar: An Overlooked Process. *Environ. Sci. Technol. Lett.* **2014**, *1* (8), 326–332.
- (4) Gelardi, D. L.; Li, C.; Parikh, S. J. An Emerging Environmental Concern: Biochar-Induced Dust Emissions and Their Potentially Toxic Properties. *Sci. Total Environ.* **2019**, *678*, 813–820.

- (5) Li, C. Y.; Bair, D. A.; Parikh, S. J. Estimating Potential Dust Emissions from Biochar Amended Soils under Simulated Tillage. *Sci. Total Environ.* **2018**, *625*, 1093–1101.
- (6) Wu, X.; Vu, T. V.; Shi, Z.; Harrison, R. M.; Liu, D.; Cen, K. Characterization and Source Apportionment of Carbonaceous PM<sub>2.5</sub> Particles in China A Review. *Atmos. Environ.* **2018**, *189*, 187–212.
- (7) Cui, H.; Mao, P.; Zhao, Y.; Nielsen, C. P.; Zhang, J. Patterns in Atmospheric Carbonaceous Aerosols in China: Emission Estimates and Observed Concentrations. *Atmos. Chem. Phys.* **2015**, *15* (15), 8657–8678.
- (8) Bond, T. C.; Doherty, S.; Fahey, D. W.; Forster, P.; Berntsen, T.; DeAngelo, B.; Flanner, M.; Ghan, S.; Kärcher, B.; Koch, D.; Kinne, S.; Kondo, Y.; Quinn, P. K.; Sarofim, M.; Schultz, M. G.; et al. Bounding the Role of Black Carbon in the Climate System: A Scientific Assessment. *J. Geophys. Res.* **2013**, *118*, 5380–5552.
- (9) Sigmund, G.; Huber, D.; Bucheli, T. D.; Baumann, M.; Borth, N.; Guebitz, G. M.; Hofmann, T. Cytotoxicity of Biochar: A Workplace Safety Concern? *Environ. Sci. Technol. Lett.* **2017**, *4* (9), 362–366
- (10) Mian, M. M.; Liu, G. Recent Progress in Biochar-Supported Photocatalysts: Synthesis, Role of Biochar, and Applications. *RSC Adv.* **2018**, *8* (26), 14237–14248.
- (11) Wang, H.; Fang, C.; Wang, Q.; Chu, Y.; Song, Y.; Chen, Y.; Xue, X. Sorption of Tetracycline on Biochar Derived from Rice Straw and Swine Manure. *RSC Adv.* **2018**, *8* (29), 16260–16268.
- (12) Tang, J.; Zhu, W.; Kookana, R.; Katayama, A. Characteristics of Biochar and Its Application in Remediation of Contaminated Soil. *J. Biosci. Bioeng.* **2013**, *116* (6), 653–659.
- (13) Zhou, Y.; Liu, Y.; Feng, L.; Xu, Y.; Du, Z.; Zhang, L. Biochar Prepared from Maize Straw and Molasses Fermentation Wastewater: Application for Soil Improvement. *RSC Adv.* **2020**, *10* (25), 14510–14519
- (14) Peterson, S. C.; Jackson, M. A.; Appell, M. Biochar: Sustainable and Versatile. In *Advances in Applied Nanotechnology for Agriculture*; American Chemical Society: Washington, DC, 2013; Vol. 1143, pp 193–205
- (15) Hale, S. E.; Lehmann, J.; Rutherford, D.; Zimmerman, A. R.; Bachmann, R. T.; Shitumbanuma, V.; O'Toole, A.; Sundqvist, K. L.; Arp, H. P.; Cornelissen, G. Quantifying the Total and Bioavailable Polycyclic Aromatic Hydrocarbons and Dioxins in Biochars. *Environ. Sci. Technol.* **2012**, *46* (5), 2830–2838.
- (16) Lieke, T.; Zhang, X.; Steinberg, C. E. W.; Pan, B. Overlooked Risks of Biochars: Persistent Free Radicals Trigger Neurotoxicity in Caenorhabditis Elegans. *Environ. Sci. Technol.* **2018**, *52* (14), 7981–7987.
- (17) Rombolà, A. G.; Meredith, W.; Snape, C. E.; Baronti, S.; Genesio, L.; Vaccari, F. P.; Miglietta, F.; Fabbri, D. Fate of Soil Organic Carbon and Polycyclic Aromatic Hydrocarbons in a Vineyard Soil Treated with Biochar. *Environ. Sci. Technol.* **2015**, 49 (18), 11037–11044.
- (18) Hilber, I.; Blum, F.; Leifeld, J.; Schmidt, H. P.; Bucheli, T. D. Quantitative Determination of PAHs in Biochar: A Prerequisite to Ensure Its Quality and Safe Application. *J. Agric. Food Chem.* **2012**, *60* (12), 3042–3050.
- (19) Chu, H.; Shang, J.; Jin, M.; Chen, Y.; Pan, Y.; Li, Y.; Tao, X.; Cheng, Z.; Meng, Q.; Li, Q.; Jia, G.; Zhu, T.; Hao, W.; Wei, X. Comparison of Lung Damage in Mice Exposed to Black Carbon Particles and 1,4-Naphthoquinone Coated Black Carbon Particles. Sci. Total Environ. 2017, 580, 572–581.
- (20) Goulaouic, S.; Foucaud, L.; Bennasroune, A.; Laval-Gilly, P.; Falla, J. Effect of Polycyclic Aromatic Hydrocarbons and Carbon Black Particles on Pro-Inflammatory Cytokine Secretion: Impact of PAH Coating onto Particles. *J. Immunotoxicol.* **2008**, *5* (3), 337–345.
- (21) Lindner, K.; Strobele, M.; Schlick, S.; Webering, S.; Jenckel, A.; Kopf, J.; Danov, O.; Sewald, K.; Buj, C.; Creutzenberg, O.; Tillmann, T.; Pohlmann, G.; Ernst, H.; Ziemann, C.; Huttmann, G.; Heine, H.; Bockhorn, H.; Hansen, T.; Konig, P.; Fehrenbach, H. Biological Effects of Carbon Black Nanoparticles Are Changed by Surface

- Coating with Polycyclic Aromatic Hydrocarbons. *Part. Fibre Toxicol.* **2017**, *14*, 8.
- (22) Pan, X.; Yuan, X.; Li, X.; Gao, S.; Sun, H.; Zhou, H.; Hou, L.; Peng, X.; Jiang, Y.; Yan, B. Induction of Inflammatory Responses in Human Bronchial Epithelial Cells by Pb<sup>2+</sup>-Containing Model PM<sub>2.5</sub> Particles *via* Downregulation of a Novel Long Noncoding RNA Inc-PCK1–2:1. *Environ. Sci. Technol.* **2019**, *53* (8), 4566–4578.
- (23) Jakab, G. J.; Risby, T. H.; Sehnert, S. S.; Hmieleski, R. R.; Gilmour, M. I. Suppression of Alveolar Macrophage Membrane-Receptor-Mediated Phagocytosis by Model Particle-Adsorbate Complexes Physicochemical Moderators of Uptake. *Environ. Health Perspect.* **1990**, *89*, 169–174.
- (24) Liu, X. L.; Ji, R.; Shi, Y.; Wang, F.; Chen, W. Release of Polycyclic Aromatic Hydrocarbons from Biochar Fine Particles in Simulated Lung Fluids: Implications for Bioavailability and Risks of Airborne Aromatics. *Sci. Total Environ.* **2019**, *655*, 1159–1168.
- (25) Mayer, P.; Hilber, I.; Gouliarmou, V.; Hale, S. E.; Cornelissen, G.; Bucheli, T. D. How to Determine the Environmental Exposure of PAHs Originating from Biochar. *Environ. Sci. Technol.* **2016**, *50* (4), 1941–1948.
- (26) de Jesus Duarte, S.; Glaser, B.; Pellegrino Cerri, C. E. Effect of Biochar Particle Size on Physical, Hydrological and Chemical Properties of Loamy and Sandy Tropical Soils. *Agronomy* **2019**, 9 (4), 165.
- (27) Chen, B.; Chen, Z. Sorption of Naphthalene and 1-Naphthol by Biochars of Orange Peels with Different Pyrolytic Temperatures. *Chemosphere* **2009**, *76* (1), 127–133.
- (28) Ahsan, M. A.; Jabbari, V.; Islam, M. T.; Turley, R. S.; Dominguez, N.; Kim, H.; Castro, E.; Hernandez-Viezcas, J. A.; Curry, M. L.; Lopez, J.; Gardea-Torresdey, J. L.; Noveron, J. C. Sustainable Synthesis and Remarkable Adsorption Capacity of MOF/Graphene Oxide and MOF/CNT Based Hybrid Nanocomposites for the Removal of Bisphenol A from Water. *Sci. Total Environ.* **2019**, *673*, 306–317.
- (29) Xiang, L.; Zeng, L.-J.; Du, P.-P.; Wang, X.-D.; Wu, X.-L.; Sarkar, B.; Lü, H.; Li, Y.-W.; Li, H.; Mo, C.-H.; Wang, H.; Cai, Q.-Y. Effects of Rice Straw Biochar on Sorption and Desorption of Di-N-Butyl Phthalate in Different Soil Particle-Size Fractions. *Sci. Total Environ.* **2020**, 702, 134878.
- (30) Zhang, C.; Zeng, G.; Huang, D.; Lai, C.; Chen, M.; Cheng, M.; Tang, W.; Tang, L.; Dong, H.; Huang, B.; Tan, X.; Wang, R. Biochar for Environmental Management: Mitigating Greenhouse Gas Emissions, Contaminant Treatment, and Potential Negative Impacts. *Chem. Eng. J.* 2019, 373, 902–922.
- (31) Nguyen, T. H.; Cho, H.-H.; Poster, D. L.; Ball, W. P. Evidence for a Pore-Filling Mechanism in the Adsorption of Aromatic Hydrocarbons to a Natural Wood Char. *Environ. Sci. Technol.* **2007**, *41* (4), 1212–1217.
- (32) Chen, B.; Zhou, D.; Zhu, L. Transitional Adsorption and Partition of Nonpolar and Polar Aromatic Contaminants by Biochars of Pine Needles with Different Pyrolytic Temperatures. *Environ. Sci. Technol.* **2008**, 42 (14), 5137–5143.
- (33) Becker, S.; Soukup, J. M.; Sioutas, C.; Cassee, F. R. Constantinos Sioutas, Flemming R Cassee, Response of Human Alveolar Macrophages to Ultrafine, Fine, and Coarse Urban Air Pollution Particles. *Exp. Lung Res.* **2003**, 29 (1), 29–44.
- (34) Bohrer, D.; Horner, R.; do Nascimento, P. C. C.; Adaime, M.; Pereira, M. E.; Martins, A. F.; Hartz, S. A. Interference in the Limulus Amebocyte Lysate Assay for Endotoxin Determination in Peritoneal Dialysis Fluids and Concentrates for Hemodialysis. *J. Pharm. Biomed. Anal.* 2001, 26, 811–818.
- (35) Qu, G.; Liu, S.; Zhang, S.; Wang, L.; Wang, X.; Sun, B.; Yin, N.; Gao, X.; Xia, T.; Chen, J.-J.; Jiang, G.-B. Graphene Oxide Induces Toll-Like Receptor 4 (TLR4)-Dependent Necrosis in Macrophages. ACS Nano 2013, 7 (7), 5732–5745.
- (36) Qu, G.; Wang, X.; Liu, S. A Crucial Role of Heme-Regulated eiF2 $\alpha$  Kinase in Maintaining Cytoskeletal Meshwork under an Oxygen Deficient Condition. *Sci. Bull.* **2017**, 62 (15), 1045–1047.

- (37) Xu, M.; Zhu, J.; Wang, F.; Xiong, Y.; Wu, Y.; Wang, Q.; Weng, J.; Zhang, Z.; Chen, W.; Liu, S. Improved *in Vitro* and *in Vivo* Biocompatibility of Graphene Oxide through Surface Modification: Poly(Acrylic Acid)-Functionalization Is Superior to Pegylation. *ACS Nano* **2016**, *10* (3), 3267–3281.
- (38) Ma, J.; Li, R.; Liu, Y.; Qu, G.; Liu, J.; Guo, W.; Song, H.; Li, X.; Liu, Y.; Xia, T.; Yan, B.; Liu, S. Carbon Nanotubes Disrupt Iron Homeostasis and Induce Anemia of Inflammation through Inflammatory Pathway as a Secondary Effect Distant to Their Portal-of-Entry. *Small* **2017**, *13* (15), 1603830.
- (39) Kim, K. H.; Jahan, S. A.; Kabir, E.; Brown, R. J. C. A Review of Airborne Polycyclic Aromatic Hydrocarbons (PAHs) and Their Human Health Effects. *Environ. Int.* **2013**, *60*, 71–80.
- (40) Hilber, I.; Mayer, P.; Gouliarmou, V.; Hale, S. E.; Cornelissen, G.; Schmidt, H. P.; Bucheli, T. D. Bioavailability and Bioaccessibility of Polycyclic Aromatic Hydrocarbons from (Post-Pyrolytically Treated) Biochars. *Chemosphere* **2017**, *174*, 700–707.
- (41) Ple, C.; Fan, Y.; Yahia, S. A.; Vorng, H.; Everaere, L.; Chenivesse, C.; Balsamelli, J.; Azzaoui, I.; de Nadai, P.; Wallaert, B.; Lazennec, G.; Tsicopoulos, A. Polycyclic Aromatic Hydrocarbons Reciprocally Regulate IL-22 and IL-17 Cytokines in Peripheral Blood Mononuclear Cells from Both Healthy and Asthmatic Subjects. *PLoS One* **2015**, *10* (4), e0122372.
- (42) Zhang, Y.; Dong, S.; Wang, H.; Tao, S.; Kiyama, R. Biological Impact of Environmental Polycyclic Aromatic Hydrocarbons (ePAHs) as Endocrine Disruptors. *Environ. Pollut.* **2016**, 213, 809–824
- (43) Ma, J.; Liu, R.; Wang, X.; Liu, Q.; Chen, Y.; Valle, R. P.; Zuo, Y. Y.; Xia, T.; Liu, S. Crucial Role of Lateral Size for Graphene Oxide in Activating Macrophages and Stimulating Pro-Inflammatory Responses in Cells and Animals. *ACS Nano* **2015**, *9* (10), 10498–10515.
- (44) Zhu, J.; Li, B.; Xu, M.; Liu, R.; Xia, T.; Zhang, Z.; Xu, Y.; Liu, S. Graphene Oxide Promotes Cancer Metastasis through Associating with Plasma Membrane to Promote Tgf-Beta Signaling-Dependent Epithelial-Mesenchymal Transition. ACS Nano 2020, 14 (1), 818–827.
- (45) Lehmann, J.; Joseph, S. Biochar for Environmental Management: Science, Technology and Implementation; Routledge: New York, 2015. (46) Zhang, Q.; Liu, X.; Meng, H.; Liu, S.; Zhang, C. Reduction Pathway-Dependent Cytotoxicity of Reduced Graphene Oxide. Environ. Sci.: Nano 2018, 5 (6), 1361–1371.
- (47) Li, R.; Wang, X.; Ji, Z.; Sun, B.; Zhang, H.; Chang, C. H.; Lin, S.; Meng, H.; Liao, Y.-P.; Wang, M.; Li, Z.; Hwang, A. A.; Song, T.-B.; Xu, R.; Yang, Y.; Zink, J. I.; Nel, A. E.; Xia, T. Surface Charge and Cellular Processing of Covalently Functionalized Multiwall Carbon Nanotubes Determine Pulmonary Toxicity. ACS Nano 2013, 7 (3), 2352–2368.
- (48) Shi, Y.; Cai, M.; Zhou, L.; Wang, H. The Structure and Function of Cell Membranes Studied by Atomic Force Microscopy. *Semin. Cell Dev. Biol.* **2018**, 73, 31–44.
- (49) Liu, Y.; Zhang, T.; Zhou, Y.; Li, J.; Liang, X.; Zhou, N.; Lv, J.; Xie, J.; Cheng, F.; Fang, Y.; Gao, Y.; Wang, N.; Huang, B. Visualization of Perforin/Gasdermin/Complement-Formed Pores in Real Cell Membranes Using Atomic Force Microscopy. *Cell. Mol. Immunol.* 2019, 16 (6), 611–620.
- (50) Sokolov, I.; Dokukin, M. E. AFM Indentation Analysis of Cells to Study Cell Mechanics and Pericellular Coat. *Methods Mol. Biol.* **2018**, *1814*, 449–468.
- (51) Zhang, H.; Fan, Q.; Wang, Y. E.; Neal, C. R.; Zuo, Y. Y. Comparative Study of Clinical Pulmonary Surfactants Using Atomic Force Microscopy. *Biochim. Biophys. Acta, Biomembr.* **2011**, *1808* (7), 1832–1842.
- (52) Zuo, Y. Y.; Veldhuizen, R. A. W.; Neumann, A. W.; Petersen, N. O.; Possmayer, F. Current Perspectives in Pulmonary Surfactant Inhibition, Enhancement and Evaluation. *Biochim. Biophys. Acta, Biomembr.* **2008**, *1778* (10), 1947–1977.
- (53) Chen, Y.; Yang, Y.; Xu, B.; Wang, S.; Li, B.; Ma, J.; Gao, J.; Zuo, Y. Y.; Liu, S. Mesoporous Carbon Nanomaterials Induced Pulmonary

- Surfactant Inhibition, Cytotoxicity, Inflammation and Lung Fibrosis. *J. Environ. Sci.* **2017**, *62*, 100–114.
- (54) Yang, Y.; Wu, Y. K.; Ren, Q. Z.; Zhang, L. G.; Liu, S. J.; Zuo, Y. Y. Biophysical Assessment of Pulmonary Surfactant Predicts the Lung Toxicity of Nanomaterials. *Small Methods* **2018**, 2 (4), 1700367.
- (55) Liu, Y.; Qi, Y.; Yin, C.; Wang, S.; Zhang, S.; Xu, A.; Chen, W.; Liu, S. Bio-Transformation of Graphene Oxide in Lung Fluids Significantly Enhances Its Photothermal Efficacy. *Nanotheranostics* **2018**, 2 (3), 222–232.
- (56) Wu, Y.; Guo, Y.; Song, H.; Liu, W.; Yang, Y.; Liu, Y.; Sang, N.; Zuo, Y. Y.; Liu, S. Oxygen Content Determines the Bio-Reactivity and Toxicity Profiles of Carbon Black Particles. *Ecotoxicol. Environ. Saf.* **2018**, *150*, 207–214.
- (57) Valle, R. P.; Wu, T.; Zuo, Y. Y. Biophysical Influence of Airborne Carbon Nanomaterials on Natural Pulmonary Surfactant. *ACS Nano* **2015**, *9* (5), 5413–5421.
- (58) Yang, Y.; Xu, L.; Dekkers, S.; Zhang, L. G.; Cassee, F. R.; Zuo, Y. Y. Aggregation State of Metal-Based Nanomaterials at the Pulmonary Surfactant Film Determines Biophysical Inhibition. *Environ. Sci. Technol.* **2018**, 52 (15), 8920–8929.
- (59) Fan, Q.; Wang, Y. E.; Zhao, X.; Loo, J. S. C.; Zuo, Y. Y. Adverse Biophysical Effects of Hydroxyapatite Nanoparticles on Natural Pulmonary Surfactant. ACS Nano 2011, 5 (8), 6410–6416.
- (60) Valle, R. P.; Huang, C. L.; Loo, J. S. C.; Zuo, Y. Y. Increasing Hydrophobicity of Nanoparticles Intensifies Lung Surfactant Film Inhibition and Particle Retention. *ACS Sustainable Chem. Eng.* **2014**, 2 (7), 1574–1580.
- (61) Hu, G.; Jiao, B.; Shi, X.; Valle, R. P.; Fan, Q.; Zuo, Y. Y. Physicochemical Properties of Nanoparticles Regulate Translocation across Pulmonary Surfactant Monolayer and Formation of Lipoprotein Corona. ACS Nano 2013, 7 (12), 10525–10533.
- (62) Hu, Q.; Bai, X.; Hu, G.; Zuo, Y. Y. Unveiling the Molecular Structure of Pulmonary Surfactant Corona on Nanoparticles. ACS Nano 2017, 11 (7), 6832–6842.
- (63) Gerber, F.; Krafft, M. P.; Vandamme, T. F.; Goldmann, M.; Fontaine, P. Preventing Crystallization of Phospholipids in Monolayers: A New Approach to Lung-Surfactant Therapy. *Angew. Chem., Int. Ed.* **2005**, 44 (18), 2749–2752.
- (64) Zhao, Q.; Li, Y.; Chai, X.; Xu, L.; Zhang, L.; Ning, P.; Huang, J.; Tian, S. Interaction of Inhalable Volatile Organic Compounds and Pulmonary Surfactant: Potential Hazards of VOCs Exposure to Lung. *J. Hazard. Mater.* **2019**, 369, 512–520.
- (65) Enkavi, G.; Javanainen, M.; Kulig, W.; Róg, T.; Vattulainen, I. Multiscale Simulations of Biological Membranes: The Challenge to Understand Biological Phenomena in a Living Substance. *Chem. Rev.* **2019**, *119* (9), 5607–5774.
- (66) Zhang, H.; Wang, Y. E.; Neal, C. R.; Zuo, Y. Y. Differential Effects of Cholesterol and Budesonide on Biophysical Properties of Clinical Surfactant. *Pediatr. Res.* **2012**, *71* (1-4), 316–323.
- (67) Leinardi, R.; Pavan, C.; Yedavally, H.; Tomatis, M.; Salvati, A.; Turci, F. Cytotoxicity of Fractured Quartz on THP-1 Human Macrophages: Role of the Membranolytic Activity of Quartz and Phagolysosome Destabilization. *Arch. Toxicol.* **2020**, *94* (9), 2981–2995
- (68) Liu, Z.; Lv, X.; Xu, L.; Liu, X.; Zhu, X.; Song, E.; Song, Y. Zinc Oxide Nanoparticles Effectively Regulate Autophagic Cell Death by Activating Autophagosome Formation and Interfering with Their Maturation. *Part. Fibre Toxicol.* **2020**, *17* (1), 46.
- (69) Ruan, X.; Sun, Y.; Du, W.; Tang, Y.; Liu, Q.; Zhang, Z.; Doherty, W.; Frost, R. L.; Qian, G.; Tsang, D. C. W. Formation, Characteristics, and Applications of Environmentally Persistent Free Radicals in Biochars: A Review. *Bioresour. Technol.* **2019**, 281, 457–468.
- (70) Liao, S. H.; Pan, B.; Li, H.; Zhang, D.; Xing, B. S. Detecting Free Radicals in Biochars and Determining Their Ability to Inhibit the Germination and Growth of Corn, Wheat and Rice Seedlings. *Environ. Sci. Technol.* **2014**, *48* (15), 8581–8587.
- (71) Dellinger, B.; Lomnicki, S.; Khachatryan, L.; Maskos, Z.; Hall, R. W.; Adounkpe, J.; McFerrin, C.; Truong, H. Formation and

- Stabilization of Persistent Free Radicals. *Proc. Combust. Inst.* **2007**, *31*, 521–528.
- (72) Loos, F.; Xie, W.; Sica, V.; Bravo-San Pedro, J. M.; Souquere, S.; Pierron, G.; Lachkar, S.; Sauvat, A.; Petrazzuolo, A.; Jimenez, A. J.; Perez, F.; Maiuri, M. C.; Kepp, O.; Kroemer, G. Artificial Tethering of LC3 or P62 to Organelles Is Not Sufficient to Trigger Autophagy. *Cell Death Dis.* **2019**, *10* (10), 771.
- (73) Deng, X.; Zhang, F.; Rui, W.; Long, F.; Wang, L.; Feng, Z.; Chen, D.; Ding, W. PM<sub>2.5</sub>-Induced Oxidative Stress Triggers Autophagy in Human Lung Epithelial A549 Cells. *Toxicol. In Vitro* **2013**, *27* (6), 1762–1770.
- (74) Pugsley, H. R. Quantifying Autophagy: Measuring LC3 Puncta and Autolysosome Formation in Cells Using Multispectral Imaging Flow Cytometry. *Methods* **2017**, *112*, 147–156.
- (75) Xia, T.; Zhu, Y.; Mu, L.; Zhang, Z. F.; Liu, S. Pulmonary Diseases Induced by Ambient Ultrafine and Engineered Nanoparticles in Twenty-First Century. *Natl. Sci. Rev.* **2016**, 3 (4), 416–429.
- (76) Ren, Q.; Wu, Y.; Ma, J.; Shan, Q.; Liu, S.; Liu, Y. Carbon Black-Induced Detrimental Effect on Osteoblasts at Low Concentrations: Remarkably Compromised Differentiation without Significant Cytotoxicity. *Ecotoxicol. Environ. Saf.* **2019**, *178*, 211–220.
- (77) Liu, J.; Wang, L.; Du, Y.; Liu, S. An Important Function of Petrosiol E in Inducing the Differentiation of Neuronal Progenitors and in Protecting Them against Oxidative Stress. *Adv. Sci.* **2017**, *4* (10), 1700089.